





C. I. Torrie,<sup>1</sup> D. Töyrä,<sup>46</sup> F. Travasso,<sup>34,35</sup> G. Traylor,<sup>7</sup> D. Trifirò,<sup>23</sup> M. C. Tringali,<sup>88,89</sup> L. Trozzo,<sup>135,21</sup> M. Tse,<sup>12</sup> M. Turconi,<sup>54</sup> D. Tuyenbayev,<sup>87</sup> D. Ugolini,<sup>136</sup> C. S. Unnikrishnan,<sup>99</sup> A. L. Urban,<sup>18</sup> S. A. Usman,<sup>37</sup> H. Vahlbruch,<sup>19</sup> G. Vajente,<sup>1</sup> G. Valdés,<sup>87</sup> N. van Bakel,<sup>11</sup> M. van Beuzekom,<sup>11</sup> J. F. J. van den Brand,<sup>63,11</sup> C. Van Den Broeck,<sup>11</sup> D. C. Vander-Hyde,<sup>37</sup> L. van der Schaaf,<sup>11</sup> J. V. van Heijningen,<sup>11</sup> A. A. van Veggel,<sup>38</sup> M. Vardaro,<sup>43,44</sup> S. Vass,<sup>1</sup> M. Vasúth,<sup>40</sup> R. Vaulin,<sup>12</sup> A. Vecchio,<sup>46</sup> G. Vedovato,<sup>44</sup> J. Veitch,<sup>46</sup> P. J. Veitch,<sup>112</sup> K. Venkateswara,<sup>137</sup> D. Verkindt,<sup>8</sup> F. Vetrano,<sup>57,58</sup> A. Viceré,<sup>57,58</sup> S. Vinciguerra,<sup>46</sup> D. J. Vine,<sup>51</sup> J.-Y. Vinet,<sup>54</sup> S. Vitale,<sup>12</sup> T. Vo,<sup>37</sup> H. Vocca,<sup>34,35</sup> C. Vorvick,<sup>39</sup> D. V. Voss,<sup>6</sup> W. D. Vousden,<sup>46</sup> S. P. Vyatchanin,<sup>50</sup> A. R. Wade,<sup>22</sup> L. E. Wade,<sup>138</sup> M. Wade,<sup>138</sup> M. Walker,<sup>2</sup> L. Wallace,<sup>1</sup> S. Walsh,<sup>31,10</sup> G. Wang,<sup>14,58</sup> H. Wang,<sup>46</sup> M. Wang,<sup>71</sup> X. Wang,<sup>52</sup> R. L. Ward,<sup>22</sup> J. Warner,<sup>39</sup> M. Was,<sup>8</sup> B. Weaver,<sup>39</sup> L.-W. Wei,<sup>54</sup> M. Weinert,<sup>10</sup> A. J. Weinstein,<sup>1</sup> R. Weiss,<sup>12</sup> L. Wen,<sup>52</sup> P. Webels,<sup>10</sup> T. Westphal,<sup>10</sup> K. Wette,<sup>10</sup> J. T. Whelan,<sup>102</sup> B. F. Whiting,<sup>6</sup> R. D. Williams,<sup>1</sup> A. R. Williamson,<sup>91</sup> J. L. Willis,<sup>139</sup> B. Willke,<sup>19,10</sup> M. H. Wimmer,<sup>10,19</sup> W. Winkler,<sup>10</sup> C. C. Wipf,<sup>1</sup> H. Wittel,<sup>10,19</sup> G. Woan,<sup>38</sup> J. Woehler,<sup>10</sup> J. Worden,<sup>39</sup> J. L. Wright,<sup>38</sup> D. S. Wu,<sup>10</sup> G. Wu,<sup>7</sup> J. Yablon,<sup>82</sup> W. Yam,<sup>12</sup> H. Yamamoto,<sup>1</sup> C. C. Yancey,<sup>64</sup> H. Yu,<sup>12</sup> M. Yvert,<sup>8</sup> A. Zadrożny,<sup>113</sup> L. Zangrandi,<sup>44</sup> M. Zanolini,<sup>98</sup> J.-P. Zendri,<sup>44</sup> M. Zevin,<sup>82</sup> L. Zhang,<sup>1</sup> M. Zhang,<sup>123</sup> Y. Zhang,<sup>102</sup> C. Zhao,<sup>52</sup> M. Zhou,<sup>82</sup> Z. Zhou,<sup>82</sup> X. J. Zhu,<sup>52</sup> M. E. Zucker,<sup>1,12</sup> S. E. Zuraw,<sup>19</sup> and J. Zweizig<sup>1</sup>

(LIGO Scientific Collaboration and Virgo Collaboration)

<sup>1</sup>*LIGO, California Institute of Technology, Pasadena, California 91125, USA*

<sup>2</sup>*Louisiana State University, Baton Rouge, Louisiana 70803, USA*

<sup>3</sup>*American University, Washington, D.C. 20016, USA*

<sup>4</sup>*Università di Salerno, Fisciano, I-84084 Salerno, Italy*

<sup>5</sup>*INFN, Sezione di Napoli, Complesso Universitario di Monte S. Angelo, I-80126 Napoli, Italy*

<sup>6</sup>*University of Florida, Gainesville, Florida 32611, USA*

<sup>7</sup>*LIGO Livingston Observatory, Livingston, Louisiana 70754, USA*

<sup>8</sup>*Laboratoire d'Annecy-le-Vieux de Physique des Particules (LAPP), Université Savoie Mont Blanc, CNRS/IN2P3, F-74941 Annecy-le-Vieux, France*

<sup>9</sup>*University of Sannio at Benevento, I-82100 Benevento, Italy  
and INFN, Sezione di Napoli, I-80100 Napoli, Italy*

<sup>10</sup>*Albert-Einstein-Institut, Max-Planck-Institut für Gravitationsphysik, D-30167 Hannover, Germany*

<sup>11</sup>*Nikhef, Science Park, 1098 XG Amsterdam, The Netherlands*

<sup>12</sup>*LIGO, Massachusetts Institute of Technology, Cambridge, Massachusetts 02139, USA*

<sup>13</sup>*Instituto Nacional de Pesquisas Espaciais, I2227-010 São José dos Campos, São Paulo, Brazil*

<sup>14</sup>*INFN, Gran Sasso Science Institute, I-67100 L'Aquila, Italy*

<sup>15</sup>*INFN, Sezione di Roma Tor Vergata, I-00133 Roma, Italy*

<sup>16</sup>*Inter-University Centre for Astronomy and Astrophysics, Pune 411007, India*

<sup>17</sup>*International Centre for Theoretical Sciences, Tata Institute of Fundamental Research, Bangalore 560012, India*

<sup>18</sup>*University of Wisconsin-Milwaukee, Milwaukee, Wisconsin 53201, USA*

<sup>19</sup>*Leibniz Universität Hannover, D-30167 Hannover, Germany*

<sup>20</sup>*Università di Pisa, I-56127 Pisa, Italy*

<sup>21</sup>*INFN, Sezione di Pisa, I-56127 Pisa, Italy*

<sup>22</sup>*Australian National University, Canberra, Australian Capital Territory 0200, Australia*

<sup>23</sup>*The University of Mississippi, University, Mississippi 38677, USA*

<sup>24</sup>*California State University Fullerton, Fullerton, California 92831, USA*

<sup>25</sup>*LAL, Univ. Paris-Sud, CNRS/IN2P3, Université Paris-Saclay, Orsay, France*

<sup>26</sup>*Chennai Mathematical Institute, Chennai 603103, India*

<sup>27</sup>*Università di Roma Tor Vergata, I-00133 Roma, Italy*

<sup>28</sup>*University of Southampton, Southampton SO17 1BJ, United Kingdom*

<sup>29</sup>*Universität Hamburg, D-22761 Hamburg, Germany*

<sup>30</sup>*INFN, Sezione di Roma, I-00185 Roma, Italy*

<sup>31</sup>*Albert-Einstein-Institut, Max-Planck-Institut für Gravitationsphysik, D-14476 Potsdam-Golm, Germany*

<sup>32</sup>*APC, Astroparticule et Cosmologie, Université Paris Diderot, CNRS/IN2P3, CEA/Irfu, Observatoire de Paris, Sorbonne Paris Cité, F-75205 Paris Cedex 13, France*

<sup>33</sup>*Montana State University, Bozeman, Montana 59717, USA*

<sup>34</sup>*Università di Perugia, I-06123 Perugia, Italy*

<sup>35</sup>*INFN, Sezione di Perugia, I-06123 Perugia, Italy*

<sup>36</sup>*European Gravitational Observatory (EGO), I-56021 Cascina, Pisa, Italy*

<sup>37</sup>*Syracuse University, Syracuse, New York 13244, USA*

<sup>38</sup>*SUPA, University of Glasgow, Glasgow G12 8QQ, United Kingdom*

- <sup>39</sup>LIGO Hanford Observatory, Richland, Washington 99352, USA  
<sup>40</sup>Wigner RCP, RMKI, H-1121 Budapest, Konkoly Thege Miklós út 29-33, Hungary  
<sup>41</sup>Columbia University, New York, New York 10027, USA  
<sup>42</sup>Stanford University, Stanford, California 94305, USA  
<sup>43</sup>Università di Padova, Dipartimento di Fisica e Astronomia, I-35131 Padova, Italy  
<sup>44</sup>INFN, Sezione di Padova, I-35131 Padova, Italy  
<sup>45</sup>CAMK-PAN, 00-716 Warsaw, Poland  
<sup>46</sup>University of Birmingham, Birmingham B15 2TT, United Kingdom  
<sup>47</sup>Università degli Studi di Genova, I-16146 Genova, Italy  
<sup>48</sup>INFN, Sezione di Genova, I-16146 Genova, Italy  
<sup>49</sup>RRCAT, Indore, MP 452013, India  
<sup>50</sup>Faculty of Physics, Lomonosov Moscow State University, Moscow 119991, Russia  
<sup>51</sup>SUPA, University of the West of Scotland, Paisley PA1 2BE, United Kingdom  
<sup>52</sup>University of Western Australia, Crawley, Western Australia 6009, Australia  
<sup>53</sup>Department of Astrophysics/IMAPP, Radboud University Nijmegen,  
P.O. Box 9010, 6500 GL Nijmegen, The Netherlands  
<sup>54</sup>Artemis, Université Côte d'Azur, CNRS, Observatoire Côte d'Azur, CS 34229, Nice cedex 4, France  
<sup>55</sup>Institut de Physique de Rennes, CNRS, Université de Rennes 1, F-35042 Rennes, France  
<sup>56</sup>Washington State University, Pullman, Washington 99164, USA  
<sup>57</sup>Università degli Studi di Urbino "Carlo Bo," I-61029 Urbino, Italy  
<sup>58</sup>INFN, Sezione di Firenze, I-50019 Sesto Fiorentino, Firenze, Italy  
<sup>59</sup>University of Oregon, Eugene, Oregon 97403, USA  
<sup>60</sup>Laboratoire Kastler Brossel, UPMC-Sorbonne Universités, CNRS, ENS-PSL Research University,  
Collège de France, F-75005 Paris, France  
<sup>61</sup>Carleton College, Northfield, Minnesota 55057, USA  
<sup>62</sup>Astronomical Observatory Warsaw University, 00-478 Warsaw, Poland  
<sup>63</sup>VU University Amsterdam, 1081 HV Amsterdam, The Netherlands  
<sup>64</sup>University of Maryland, College Park, Maryland 20742, USA  
<sup>65</sup>Center for Relativistic Astrophysics and School of Physics, Georgia Institute of Technology,  
Atlanta, Georgia 30332, USA  
<sup>66</sup>Laboratoire des Matériaux Avancés (LMA), CNRS/IN2P3, F-69622 Villeurbanne, France  
<sup>67</sup>Université Claude Bernard Lyon 1, F-69622 Villeurbanne, France  
<sup>68</sup>Università di Napoli "Federico II," Complesso Universitario di Monte S.Angelo, I-80126 Napoli, Italy  
<sup>69</sup>NASA/Goddard Space Flight Center, Greenbelt, Maryland 20771, USA  
<sup>70</sup>RESCEU, University of Tokyo, Tokyo 113-0033, Japan  
<sup>71</sup>Tsinghua University, Beijing 100084, China  
<sup>72</sup>Texas Tech University, Lubbock, Texas 79409, USA  
<sup>73</sup>National Tsing Hua University, Hsinchu City, 30013 Taiwan, Republic of China  
<sup>74</sup>Charles Sturt University, Wagga Wagga, New South Wales 2678, Australia  
<sup>75</sup>West Virginia University, Morgantown, West Virginia 26506, USA  
<sup>76</sup>University of Chicago, Chicago, Illinois 60637, USA  
<sup>77</sup>Caltech CaRT, Pasadena, California 91125, USA  
<sup>78</sup>Korea Institute of Science and Technology Information, Daejeon 305-806, Korea  
<sup>79</sup>Università di Roma "La Sapienza," I-00185 Roma, Italy  
<sup>80</sup>University of Brussels, Brussels 1050, Belgium  
<sup>81</sup>Sonoma State University, Rohnert Park, California 94928, USA  
<sup>82</sup>Center for Interdisciplinary Exploration & Research in Astrophysics (CIERA), Northwestern University,  
Evanston, Illinois 60208, USA  
<sup>83</sup>University of Minnesota, Minneapolis, Minnesota 55455, USA  
<sup>84</sup>The University of Melbourne, Parkville, Victoria 3010, Australia  
<sup>85</sup>Institute for Plasma Research, Bhat, Gandhinagar 382428, India  
<sup>86</sup>The University of Sheffield, Sheffield S10 2TN, United Kingdom  
<sup>87</sup>The University of Texas Rio Grande Valley, Brownsville, Texas 78520, USA  
<sup>88</sup>Università di Trento, Dipartimento di Fisica, I-38123 Povo, Trento, Italy  
<sup>89</sup>INFN, Trento Institute for Fundamental Physics and Applications, I-38123 Povo, Trento, Italy  
<sup>90</sup>The Pennsylvania State University, University Park, Pennsylvania 16802, USA  
<sup>91</sup>Cardiff University, Cardiff CF24 3AA, United Kingdom  
<sup>92</sup>Montclair State University, Montclair, New Jersey 07043, USA  
<sup>93</sup>MTA Eötvös University, "Lendulet" Astrophysics Research Group, Budapest 1117, Hungary

- <sup>94</sup>National Astronomical Observatory of Japan,  
2-21-1 Osawa, Mitaka, Tokyo 181-8588, Japan
- <sup>95</sup>School of Mathematics, University of Edinburgh, Edinburgh EH9 3FD, United Kingdom
- <sup>96</sup>Indian Institute of Technology, Gandhinagar, Ahmedabad, Gujarat 382424, India
- <sup>97</sup>University of Szeged, Dóm tér 9, Szeged 6720, Hungary
- <sup>98</sup>Embry-Riddle Aeronautical University, Prescott, Arizona 86301, USA
- <sup>99</sup>Tata Institute of Fundamental Research, Mumbai 400005, India
- <sup>100</sup>INAF, Osservatorio Astronomico di Capodimonte, I-80131 Napoli, Italy
- <sup>101</sup>University of Michigan, Ann Arbor, Michigan 48109, USA
- <sup>102</sup>Rochester Institute of Technology, Rochester, New York 14623, USA
- <sup>103</sup>NCSA, University of Illinois at Urbana-Champaign, Urbana, Illinois 61801, USA
- <sup>104</sup>Universitat de les Illes Balears, IAC3—IEEC, E-07122 Palma de Mallorca, Spain
- <sup>105</sup>University of Białystok, 15-424 Białystok, Poland
- <sup>106</sup>SUPA, University of Strathclyde, Glasgow G1 1XQ, United Kingdom
- <sup>107</sup>IISER-TVM, CET Campus, Trivandrum, Kerala 695016, India
- <sup>108</sup>Canadian Institute for Theoretical Astrophysics, University of Toronto,  
Toronto, Ontario M5S 3H8, Canada
- <sup>109</sup>Institute of Applied Physics, Nizhny Novgorod 603950, Russia
- <sup>110</sup>Pusan National University, Busan 609-735, Korea
- <sup>111</sup>Hanyang University, Seoul 133-791, Korea
- <sup>112</sup>University of Adelaide, Adelaide, South Australia 5005, Australia
- <sup>113</sup>NCBJ, 05-400 Świerk-Otwock, Poland
- <sup>114</sup>IM-PAN, 00-956 Warsaw, Poland
- <sup>115</sup>Monash University, Victoria 3800, Australia
- <sup>116</sup>Seoul National University, Seoul 151-742, Korea
- <sup>117</sup>The Chinese University of Hong Kong, Shatin, NT, Hong Kong SAR, China
- <sup>118</sup>University of Alabama in Huntsville, Huntsville, Alabama 35899, USA
- <sup>119</sup>University of Massachusetts-Amherst, Amherst, Massachusetts 01003, USA
- <sup>120</sup>ESPCI, CNRS, F-75005 Paris, France
- <sup>121</sup>Università di Camerino, Dipartimento di Fisica, I-62032 Camerino, Italy
- <sup>122</sup>Southern University and A&M College, Baton Rouge, Louisiana 70813, USA
- <sup>123</sup>College of William and Mary, Williamsburg, Virginia 23187, USA
- <sup>124</sup>Instituto de Física Teórica, University Estadual Paulista/ICTP
- South American Institute for Fundamental Research, São Paulo, SP 01140-070, Brazil
- <sup>125</sup>University of Cambridge, Cambridge CB2 1TN, United Kingdom
- <sup>126</sup>IISER-Kolkata, Mohanpur, West Bengal 741252, India
- <sup>127</sup>Rutherford Appleton Laboratory, HSIC, Chilton, Didcot, Oxon OX11 0QX, United Kingdom
- <sup>128</sup>Whitman College, 345 Boyer Avenue, Walla Walla, Washington 99362, USA
- <sup>129</sup>National Institute for Mathematical Sciences, Daejeon 305-390, Korea
- <sup>130</sup>Université de Lyon, F-69361 Lyon, France
- <sup>131</sup>Hobart and William Smith Colleges, Geneva, New York 14456, USA
- <sup>132</sup>Janusz Gil Institute of Astronomy, University of Zielona Góra, 65-265 Zielona Góra, Poland
- <sup>133</sup>King's College London, University of London, London WC2R 2LS, United Kingdom
- <sup>134</sup>Andrews University, Berrien Springs, Michigan 49104, USA
- <sup>135</sup>Università di Siena, I-53100 Siena, Italy
- <sup>136</sup>Trinity University, San Antonio, Texas 78212, USA
- <sup>137</sup>University of Washington, Seattle, Washington 98195, USA
- <sup>138</sup>Kenyon College, Gambier, Ohio 43022, USA
- <sup>139</sup>Abilene Christian University, Abilene, Texas 79699, USA

(Received 14 May 2016; published 15 August 2016)

We report on a comprehensive all-sky search for periodic gravitational waves in the frequency band 100–1500 Hz and with a frequency time derivative in the range of  $[-1.18, +1.00] \times 10^{-8}$  Hz/s. Such a signal could be produced by a nearby spinning and slightly nonaxisymmetric isolated neutron star in our galaxy. This search uses the data from the initial LIGO sixth science run and covers a larger parameter space with respect to any past search. A *Loosely Coherent* detection pipeline was applied to follow up weak outliers in both Gaussian (95% recovery rate) and non-Gaussian (75% recovery rate) bands. No gravitational wave signals were observed, and upper limits were placed on their strength. Our smallest

\*Deceased

upper limit on worst-case (linearly polarized) strain amplitude  $h_0$  is  $9.7 \times 10^{-25}$  near 169 Hz, while at the high end of our frequency range we achieve a worst-case upper limit of  $5.5 \times 10^{-24}$ . Both cases refer to all sky locations and entire range of frequency derivative values.

DOI: 10.1103/PhysRevD.94.042002

## I. INTRODUCTION

In this paper we report the results of a comprehensive all-sky search for continuous, nearly monochromatic gravitational waves in data from LIGO's sixth science (S6) run. The search covered frequencies from 100 Hz through 1500 Hz and frequency derivatives from  $-1.18 \times 10^{-8}$  Hz/s through  $1.00 \times 10^{-8}$  Hz/s.

A number of searches for periodic gravitational waves have been carried out previously in LIGO data [1–10], including coherent searches for gravitational radiation from known radio and X-ray pulsars. An Einstein@Home search running on the BOINC infrastructure [11] has performed blind all-sky searches on S4 and S5 data [12–14].

The results in this paper were produced with the PowerFlux search program. It was first described in [1] together with two other semicoherent search pipelines (Hough, Stackslide). The sensitivities of all three methods were compared, with PowerFlux showing better results in frequency bands lacking severe spectral artifacts. A subsequent article [3] based on the data from the S5 run featured improved upper limits and a systematic outlier follow-up search based on the *Loosely Coherent* algorithm [15].

The analysis of the data set from the sixth science run described in this paper has several distinguishing features from previously published results:

- (i) A number of upgrades to the detector were made in order to field-test the technology for Advanced LIGO interferometers. This resulted in a factor of about two improvement in intrinsic noise level at high frequencies compared to previously published results [3].
- (ii) The higher sensitivity allowed us to use less data while still improving upper limits in high frequency bands by 25% over previously published results. This smaller data set allowed covering larger parameter space, and comprehensive exploration of high frequency data.
- (iii) This search improved on previous analyses by partitioning the data in  $\approx 1$  month chunks and looking for signals in any contiguous sequence of these chunks. This enables detections of signals that conform to ideal signal model over only part of the data. Such signals could arise because of a glitch, or because of influence of a long-period companion object.
- (iv) The upgrades to the detector, while improving sensitivity on average, introduced a large number of detector artifacts, with 20% of frequency range contaminated by non-Gaussian noise. We addressed

this issue by developing a new *universal statistic* [16] that provides correct upper limits regardless of the noise distribution of the underlying data, while still showing close to optimal performance for Gaussian data.

We have observed no evidence of gravitational radiation and have established the most sensitive upper limits to date in the frequency band 100–1500 Hz. Our smallest 95% confidence level upper limit on worst-case (linearly polarized) strain amplitude  $h_0$  is  $9.7 \times 10^{-25}$  near 169 Hz, while at the high end of our frequency range we achieve a worst-case upper limit of  $5.5 \times 10^{-24}$ . Both cases refer to all sky locations and entire range of frequency derivative values.

## II. LIGO INTERFEROMETERS AND S6 SCIENCE RUN

The LIGO gravitational wave network consists of two observatories, one in Hanford, Washington and the other in Livingston, Louisiana, separated by a 3000 km baseline. During the S6 run each site housed one suspended interferometer with 4 km long arms.

While the sixth science run spanned a  $\approx 15$  months period of data acquisition, this analysis used only data from GPS 951534120 (2010 Mar 02 03:01:45 UTC) through GPS 971619922 (2010 Oct 20 14:25:07 UTC), for which strain sensitivity was best. Since interferometers sporadically fall out of operation (“lose lock”) due to environmental or instrumental disturbances or for scheduled maintenance periods, the data set was not contiguous. The Hanford interferometer H1 had a duty factor of 53%, while the Livingston interferometer L1 had a duty factor of 51%. The strain sensitivity was not uniform, exhibiting a  $\sim 50\%$  daily variation from anthropogenic activity as well as gradual improvement toward the end of the run [17,18].

Nonstationarity of noise was especially severe at frequencies below 100 Hz, and since the average detector sensitivity for such frequencies was not significantly better than that observed in the longer S5 run [3], this search was restricted to frequencies above 100 Hz.

A detailed description of the instruments and data can be found in [19].

## III. THE SEARCH FOR CONTINUOUS GRAVITATIONAL RADIATION

### A. Overview

In this paper we assume a classical model of a spinning neutron star with a rotating quadrupole moment that

produces circularly polarized gravitational radiation along the rotation axis and linearly polarized radiation in the directions perpendicular to the rotation axis. The linear polarization is the worst case as such signals contribute the smallest amount of power to the detector.

The strain signal template is assumed to be

$$h(t) = h_0 \left( F_+(t, \alpha_0, \delta_0, \psi) \frac{1 + \cos^2(\iota)}{2} \cos(\Phi(t)) + F_\times(t, \alpha_0, \delta_0, \psi) \cos(\iota) \sin(\Phi(t)) \right), \quad (1)$$

where  $F_+$  and  $F_\times$  characterize the detector responses to signals with “+” and “×” quadrupolar polarizations [1–3], the sky location is described by right ascension  $\alpha_0$  and declination  $\delta_0$ , the inclination of the source rotation axis to the line of sight is denoted  $\iota$ , and the phase evolution of the signal is given by the formula

$$\Phi(t) = 2\pi(f_{\text{source}} \cdot (t - t_0) + f^{(1)} \cdot (t - t_0)^2/2) + \phi, \quad (2)$$

with  $f_{\text{source}}$  being the source frequency and  $f^{(1)}$  denoting the first frequency derivative (which, when negative, is termed the *spindown*). We use  $t$  to denote the time in the Solar System barycenter frame. The initial phase  $\phi$  is computed relative to reference time  $t_0$ . When expressed as a function of local time of ground-based detectors Eq. (2) acquires sky-position-dependent Doppler shift terms. We use  $\psi$  to denote the polarization angle of the projected source rotation axis in the sky plane.

The search has two main components. First, the main *PowerFlux* algorithm [1–3,20–22] was run to establish upper limits and produce lists of outliers with signal-to-noise ratio (SNR) greater than 5. Next, the *Loosely Coherent* detection pipeline [3,15,23] was used to reject or confirm collected outliers.

Both algorithms calculate power for a bank of signal model templates and compute upper limits and signal-to-noise ratios for each template based on comparison to templates with nearby frequencies and the same sky location and spindown. The input time series is broken into 50% overlapping 1800 s long segments which are Hann windowed and Fourier transformed. The resulting short Fourier transforms (SFTs) are arranged into an input matrix with time and frequency dimensions. The power calculation can be expressed as a bilinear form of the input matrix  $\{a_{t,f}\}$ :

$$P[f] = \sum_{t_1, t_2} a_{t_1, f + \delta f(t_1)} a_{t_2, f + \delta f(t_2)}^* K_{t_1, t_2, f} \quad (3)$$

Here  $\delta f(t)$  denotes the detector frame frequency drift due to the effects from both Doppler shifts and the first frequency derivative. The sum is taken over all times  $t$  corresponding to the midpoint of the short Fourier transform time interval.

The kernel  $K_{t_1, t_2, f}$  includes the contribution of time dependent SFT weights, antenna response, signal polarization parameters and relative phase terms [15,23].

The main semi-coherent PowerFlux algorithm uses a kernel with main diagonal terms only and is very fast. The Loosely Coherent algorithms increase coherence time while still allowing for controlled deviation in phase [15]. This is done by more complicated kernels that increase effective coherence length.

The effective coherence length is captured in a parameter  $\delta$ , which describes the amount of phase drift that the kernel allows between SFTs, with  $\delta = 0$  corresponding to a fully coherent case, and  $\delta = 2\pi$  corresponding to incoherent power sums.

Depending on the terms used, the data from different interferometers can be combined incoherently (such as in stages 0 and 1, see Table II) or coherently (as used in stages 2, 3 and 4). The coherent combination is more computationally expensive but provides much better parameter estimation.

The upper limits (Fig. 1) are reported in terms of the worst-case value of  $h_0$  (which applies to linear polarizations with  $\iota = \pi/2$ ) and for the most sensitive circular polarization ( $\iota = 0$  or  $\pi$ ). As described in the previous paper [3], the pipeline does retain some sensitivity, however, to non-general-relativity GW polarization models, including a longitudinal component, and to slow amplitude evolution.

The 95% confidence level upper limits (see Fig. 1) produced in the first stage are based on the overall noise level and largest outlier in strain found for every template in each 0.25 Hz band in the first stage of the pipeline. The 0.25 Hz bands are analyzed by separate instances of PowerFlux [3]. A followup search for detection is carried out for high-SNR outliers found in the first stage. Certain frequency ranges (Table I) were excluded from the analysis because of gross contamination by detector artifacts.

## B. Universal statistics

The detector sensitivity upgrades introduced many artifacts, so that in 20% of the sensitive frequency range the noise follows non-Gaussian distributions which, in addition, are unknown. As the particular non-Gaussian distribution can vary widely depending on particular detector artifacts, the ideal estimate based on full knowledge of the distribution is not usually available. In the previous analysis [1–3], the frequency bands where the noise distribution was non-Gaussian were not used to put upper limits. However, in the present case this approach would have resulted in excluding most of the frequency bands below 400 Hz and many above 400 Hz; even though the average strain sensitivity in many of these frequency bands is better than in the past.

To make use of the entire spectrum, we used in this work the *Universal statistic* algorithm [16] for establishing upper limits. The algorithm is derived from the Markov inequality

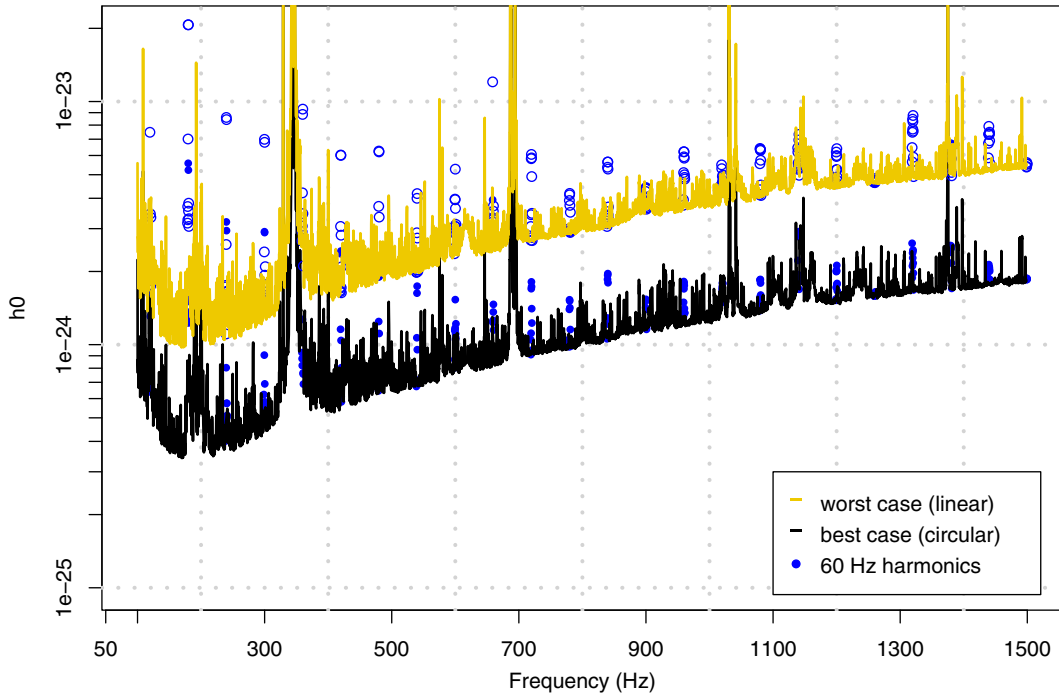


FIG. 1. S6 upper limits. The upper (yellow) curve shows worst-case (linearly polarized) 95% CL upper limits in analyzed 0.25 Hz bands (see Table I for list of excluded bands). The lower (grey) curve shows upper limits assuming a circularly polarized source. The values of solid points and circles mark frequencies within 1.25 Hz of 60 Hz power line harmonics for circularly (solid points) and linearly (open circles) polarized sources. The data for this plot can be found in [24].

and shares its independence from the underlying noise distribution. It produces upper limits less than 5% above optimal in case of Gaussian noise. In non-Gaussian bands it can report values larger than what would be obtained if the distribution were known, but the upper limits are always at least 95% valid. Figure 2 shows results of an injection run performed as described in [3]. Correctly established upper limits are above the red line.

### C. Detection pipeline

The detection pipeline used in [3] was extended with additional stages (see Table II) to winnow the larger number of initial outliers, expected because of non-Gaussian artifacts and larger initial search space. This detection pipeline was also used in the search of the Orion spur [4].

TABLE I. Frequency regions excluded from upper limit analysis. “Violin modes” are resonant vibrations of the wires which suspend the many mirrors of the interferometer.

Category	Description
First harmonic of violin modes	343.25–343.75 Hz, 347–347.25 Hz
Second harmonic of violin modes	686.25–687.5 Hz
Third harmonic of violin modes	1031.00–1031.25 Hz

The initial stage (marked 0) scans the entire sky with semicoherent algorithm that computes weighted sums of powers of 1800 s Hann-windowed SFTs. These power sums are then analyzed to identify high-SNR outliers. A

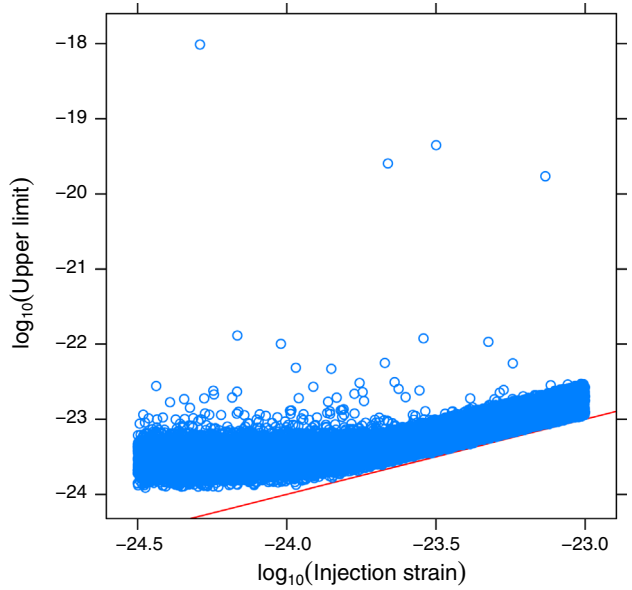


FIG. 2. Upper limit validation. Each point represents a separate injection in the 400–1500 Hz frequency range. Each established upper limit (vertical axis) is compared against the injected strain value (horizontal axis, red line).

TABLE II. Analysis pipeline parameters. Starting with stage 1, all stages used the Loosely Coherent algorithm for demodulation. The sky and frequency refinement parameters are relative to values used in the semicoherent PowerFlux search.

Stage	Instrument sum	Phase coherence rad	Spindown step Hz/s	Sky refinement	Frequency refinement	SNR increase %
0	Initial/upper limit semicoherent	NA	$2 \times 10^{-10}$	1	1/2	NA
1	Incoherent	$\pi/2$	$1.0 \times 10^{-10}$	1/4	1/8	20
2	Coherent	$\pi/2$	$5.0 \times 10^{-11}$	1/4	1/8	0
3	Coherent	$\pi/4$	$2.5 \times 10^{-11}$	1/8	1/16	12
4	Coherent	$\pi/8$	$5.0 \times 10^{-12}$	1/16	1/32	12

separate algorithm uses universal statistics [16] to establish upper limits.

The entire data set was partitioned into 7 segments of equal length and power sums were produced independently for any contiguous combinations of these stretches. As in [4] the outlier identification was performed independently in each stretch.

High-SNR outliers were subject to a coincidence test. For each outlier with  $\text{SNR} > 7$  in the combined H1 and L1 data, we required there to be outliers in the individual detector data that had  $\text{SNR} > 5$ , matching the parameters of the combined-detector outlier within a distance of  $0.03 \text{ rad} \cdot 400 \text{ Hz}/f$  on the sky,  $2 \text{ mHz}$  in frequency, and  $3 \times 10^{-10} \text{ Hz/s}$  in spindown. However, the combined-detector SNR could not be *lower* than either single-detector SNR.

The identified outliers using combined data are then passed to followup stage using Loosely Coherent algorithm [15] with progressively tighter phase coherence parameters  $\delta$ , and improved determination of frequency, spindown and sky location.

As the initial stage 0 only sums powers it does not use relative phase between interferometers, which results in some degeneracy between sky position, frequency and spindown. The first Loosely Coherent followup stage also combines interferometer powers incoherently, but demands greater temporal coherence (smaller  $\delta$ ) within each interferometer, which should boost SNR of viable outliers by at least 20%. Subsequent stages use data coherently providing tighter bounds on outlier location.

The testing of the pipeline was done above 400 Hz and included both Gaussian and non-Gaussian bands. We focused on high frequency performance because preliminary S6 data indicated the sensitivity at low frequencies was unlikely to improve over S5 results due to detector artifacts.

The followup code was tested to recover 95% of injections 50% above the upper limit level assuming uniform distribution of injection frequency (Fig. 3). Recovery of signals injected into frequency bands which exhibits non-Gaussian noise was 75% (Fig. 4). Our recovery criterion demanded that an outlier close to the true injection location (within 2 mHz in frequency  $f$ ,

$3 \times 10^{-10} \text{ Hz/s}$  in spindown and  $12 \text{ rad} \cdot \text{Hz}/f$  in sky location) be found and successfully pass through all stages of the detection pipeline. As each stage of the pipeline only passes outliers with an increase in SNR, this resulted in an outlier that strongly stood out above the background, with good estimates of the parameters of the underlying signal.

It should be noted that the injection recovery curve in Fig. 3 passes slightly below the 95% level for  $h_0$  equal to the upper limit. However, the upper limits are based on power levels measured by stage 0, independent of any follow-up criteria. That is, we can say with 95% confidence that a signal above the upper limit level is inconsistent with the observed power, even though such a (hypothetical) signal might not pass all of our follow-up criteria to be “detected.” The main reason that these injections fail to be detected is the different sensitivities of the H1 and L1

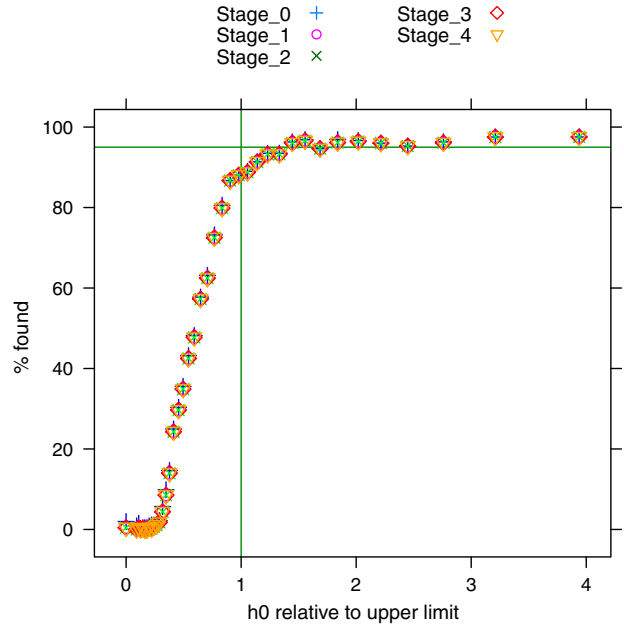


FIG. 3. Injection recovery in frequency bands above 400 Hz. The injected strain divided by the upper limit in this band (before injection) is shown on the horizontal axis. The percentage of surviving injections is shown on the vertical axis, with horizontal line drawn at 95% level. Stage 0 is the output of the coincidence test after the initial semicoherent search.

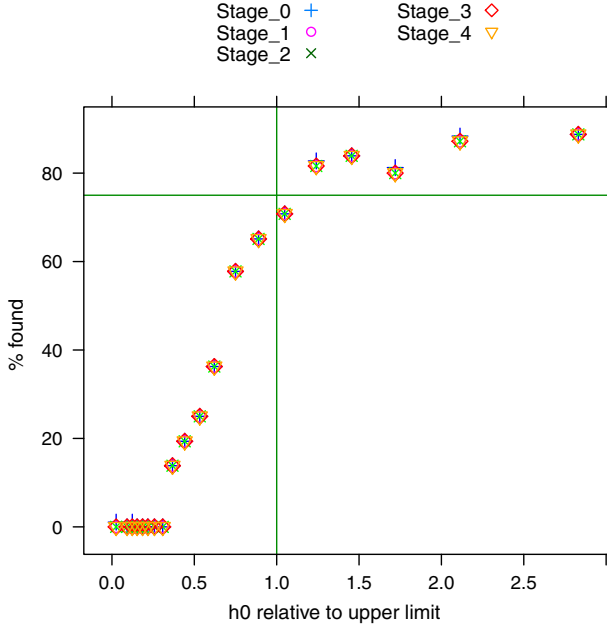


FIG. 4. Injection recovery in non-Gaussian bands above 400 Hz. The injected strain divided by the upper limit in this band (before injection) is shown on the horizontal axis. The percentage of surviving injections is shown on the vertical axis, with horizontal line drawn at 75% level.

detectors. When one interferometer is less sensitive we can still set a good upper limit, but the initial coincidence criteria requires that an outlier be marginally seen in both interferometers. In the previous analysis [3] the interferometers had similar sensitivity and the curve passed through the intersection of the green lines (horizontal axis value of 1, vertical axis value of 95%).

#### D. Gaussian false alarm event rate

The computation of the false alarm rate for the outliers passing all stages of the pipeline is complicated by the fact that most outliers are caused by instrumental artifacts for which we do not know the underlying probability distribution. In principle, one could repeat the analysis many times using nonphysical frequency shifts (which would exclude picking up a real signal by accident) in order to obtain estimates of false alarm rate, but this approach is very computationally expensive. Even assuming a perfect Gaussian background, it is difficult to analytically model the pipeline in every detail to obtain an accurate estimate of the false alarm rate, given the gaps in interferometer operations and nonstationary noise.

Instead, following [4], we compute a figure of merit that overestimates the actual Gaussian false alarm event rate. We simplify the problem by assuming that the entire analysis was carried out with the resolution of the very last stage of follow-up and we are merely triggering on the SNR value of the last stage. This is extremely conservative as we ignore the consistency requirements that allow the

outlier to proceed from one stage of the pipeline to the next; the actual false alarm rate could be lower.

The SNR of each outlier is computed relative to the Loosely Coherent power sum for 501 frequency bins spaced at 1/1800 Hz intervals (including the outlier) but with all the other signal parameters held constant. The spacing assures that correlations between neighboring sub-bins do not affect the statistics of the power sum.

To simplify computation we assume that we are dealing with a simple  $\chi^2$  distribution with the number of degrees of freedom given by the timebase divided by the coherence length and multiplied by a conservative duty factor reflecting interferometer uptime and the worst-case weights from linearly-polarized signals.

Thus to find the number  $N$  of degrees of freedom we will use the formula

$$N \approx \frac{\text{timebase} \cdot \delta \cdot \text{duty factor}}{1800 \text{ s} \cdot 2\pi} \quad (4)$$

with the duty factor taken to be 0.125 and  $\delta$  giving the phase coherence parameter of the Loosely Coherent search. The duty factor was chosen to allow for only 50% interferometer uptime and only one quarter of the data receiving high weights from our procedure, which weights the contribution of data inversely as the square of the estimated noise [20,21].

Thus we define the outlier figure of merit describing Gaussian false alarm (GFA) event rate as

$$\text{GFA} = K \cdot P_{\chi^2}(N + \text{SNR} \cdot \sqrt{2N}; N) \quad (5)$$

where  $N$  defines the number of degrees of freedom as given by equation (4),  $P_{\chi^2}(x; N)$  gives the probability for a  $\chi^2$  distribution with  $N$  degrees of freedom to exceed  $x$ , and  $K = 1.3 \times 10^{14}$  is the estimated number of templates.

We point out that the GFA is overly conservative when applied to frequency bands with Gaussian noise, but is only loosely applicable to bands with detector artifacts, which can affect both the estimate of the number of degrees of freedom of the underlying distribution and the assumption of uncorrelated underlying noise.

## IV. RESULTS

The PowerFlux algorithm and Loosely Coherent method compute power estimates for gravitational waves in a given frequency band for a fixed set of templates. The template parameters usually include frequency, first frequency derivative and sky location.

Since the search target is a rare monochromatic signal, it would contribute excess power to one of the frequency bins after demodulation. The upper limit on the maximum excess relative to the nearby power values can then be established. For this analysis we use a universal statistic [16] that places conservative 95% confidence level upper

limits for an arbitrary statistical distribution of noise power. The universal statistic has been designed to provide close to optimal values in the common case of Gaussian distribution.

The PowerFlux algorithm and Loosely Coherent method have been described in detail in [1,2,15,20–22].

Most natural sources are expected to have negative first frequency derivative, as the energy lost in gravitational or electromagnetic waves would make the source spin more slowly. The frequency derivative can be positive when the source is affected by a strong slowly-variable Doppler shift, such as due to a long-period orbit.

The large gap in data taking due to installation of Advanced LIGO interferometers provided an opportunity to cover an extended parameter space (Fig. 5). With respect to previous searches, we have chosen to explore comprehensively both negative and positive frequency derivatives to avoid missing any unexpected sources in our data.

The upper limits obtained in the search are shown in Fig. 1. The numerical data for this plot can be obtained separately [24]. The upper (yellow) curve shows the upper limits for a worst-case (linear) polarizations when the smallest amount of gravitational energy is projected toward Earth. The lower curve shows upper limits for an optimally oriented source. Because of the day-night variability of the interferometer sensitivity due to anthropogenic noise, the linearly polarized sources are more susceptible to detector artifacts, as the detector response to such sources varies with the same period. The neighborhood of 60 Hz harmonics is shown as circles for worst case upper limits and dots for circular polarization upper limits. Thanks to the use of universal statistic they do represent valid values even if contaminated by human activity.

Each point in Fig. 1 represents a maximum over the sky: only a small excluded portion of the sky near ecliptic poles

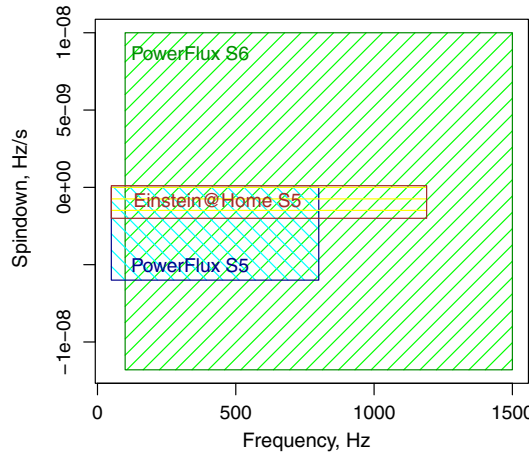


FIG. 5. Parameter space covered in the analysis. Einstein@Home searches use longer coherence times than PowerFlux, with better sensitivity to narrow band signals. The results for area marked “PowerFlux S6” are reported in this paper.

that is highly susceptible to detector artifacts, due to stationary frequency evolution produced by the combination of frequency derivative and Doppler shifts. The exclusion procedure is described in [3] and applied to 0.033% of the sky over the entire run.

A few frequency bands shown in Table I were so contaminated that every SFT was vetoed by data conditioning code and the analysis terminated before reaching universal statistic stage. While the universal statistic could have established upper limits with veto turned off, we opted to simply exclude these bands, as the contamination would raise upper limits to be above physically interesting values.

If one assumes that the source spindown is solely due to emission of gravitational waves, then it is possible to recast upper limits on source amplitude as a limit on source ellipticity. Figure 6 shows the reach of our search under different assumptions on source distance. Superimposed are lines corresponding to sources of different ellipticities.

The detection pipeline produced 16 outliers (Table III). Each outlier is identified by a numerical index. We report SNR, decimal logarithm of Gaussian false alarm rate, as well as frequency, spindown and sky location.

The “Segment” column describes the persistence of the outlier through the data, and specified which contiguous subset of the 7 equal partitions of the timespan contributed most significantly to the outlier: see [4] for details. A continuous signal will normally have [0, 6] in this column (similar contribution from all 7 segments), or on rare

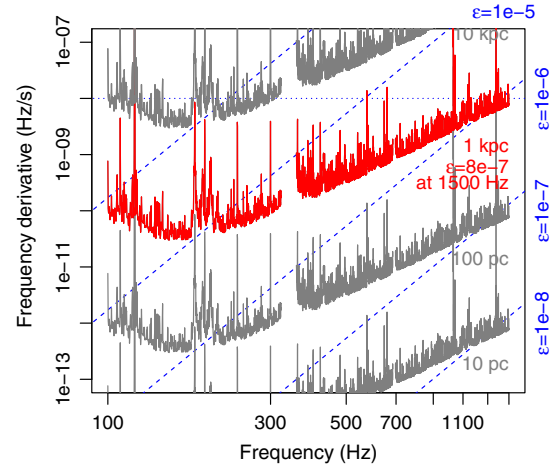


FIG. 6. Range of the PowerFlux search for neutron stars spinning down solely due to gravitational radiation. This is a superposition of two contour plots. The grey and red solid lines are contours of the maximum distance at which a neutron star could be detected as a function of gravitational-wave frequency  $f$  and its derivative  $\dot{f}$ . The dashed lines are contours of the corresponding ellipticity  $\epsilon(f, \dot{f})$ . The fine dotted line marks the maximum spindown searched. Together these quantities tell us the maximum range of the search in terms of various populations (see text for details).

TABLE III. Outliers that passed detection pipeline. Only the highest-SNR outlier is shown for each 0.1 Hz frequency region. Outliers marked with “line” had strong narrowband disturbances identified near the outlier location. Outliers marked as “non-Gaussian” were identified as having non-Gaussian statistics in their power sums, often due to a very steeply sloping spectrum. GFA is the Gaussian false alarm figure of merit described in Sec. III D. Segment column reports the set of contiguous segments of the data that produced the outlier, as described in IV. Frequencies are converted to epoch GPS 961577021.

Idx	SNR	$\log_{10}(\text{GFA})$	Segment	Frequency Hz	Spindown nHz/s	$\text{RA}_{\text{J}2000}$ degrees	$\text{DEC}_{\text{J}2000}$ degrees	Description
1	3331	-9360	[0, 6]	192.49269	-8.650	351.371	-33.342	Hardware injection ip8
21	1329	-3114	[1, 5]	108.85717	-0.000	178.417	-33.400	Hardware injection ip3, Non-Gaussian, disturbed H1 spectrum
42	957	-2622	[0, 6]	575.16354	0.005	215.261	3.370	Hardware injection ip2
69	112	-196	[0, 3]	397.51894	-0.115	271.698	67.257	Non-Gaussian, Line in H1, disturbed spectrum in L1
72	93	-78	[4, 4]	1397.76097	-11.220	296.704	-16.069	Induced by loud hardware injection ip4, Non-Gaussian, highly disturbed H1 + L1 spectra
76	82	-162	[0, 5]	1145.20043	0.400	90.936	-67.610	Highly disturbed H1 spectrum, stationary line area
79	64	-98	[1, 4]	566.08359	-4.850	91.028	86.915	Line in H1 at 566.085 Hz
81	54	-68	[2, 4]	704.03500	4.110	117.932	50.411	Disturbed H1 and L1 spectrum
82	48	-86	[0, 6]	1220.74448	-1.120	223.413	-20.502	Hardware injection ip7, sloping H1 and L1 spectra
83	48	-73	[0, 4]	140.41014	-0.010	270.298	66.821	Highly disturbed H1 spectrum, stationary line area
94	36	-44	[0, 3]	192.65413	9.270	145.440	10.439	Induced by loud hardware injection ip8
95	35	-28	[2, 3]	250.01082	2.750	247.459	-76.842	Lines in H1 and L1, Non-Gaussian
101	19	-13	[2, 6]	1145.30312	8.515	196.471	33.778	Highly disturbed H1 spectrum
102	18	-12	[0, 4]	1397.91328	1.070	42.627	32.827	Induced by loud hardware injection ip4, Non-Gaussian, highly disturbed H1 + L1 spectra
103	17	-4	[3, 4]	1143.41710	-2.455	107.611	-56.347	Highly disturbed H1 spectrum
107	14	-0	[2, 3]	451.47993	-10.880	49.317	33.890	Line in H1 at 451.5 Hz

TABLE IV. Parameters of hardware-injected simulated signals detected by PowerFlux (epoch GPS 961577021).

Label	Frequency Hz	Spindown nHz/s	$\text{RA}_{\text{J}2000}$ degrees	$\text{DEC}_{\text{J}2000}$ degrees
ip2	575.163 54	$-1.37 \times 10^{-4}$	215.256 17	3.4440
ip3	108.857 16	$-1.46 \times 10^{-8}$	178.372 57	-33.4366
ip4	1397.831 947	-25.4	4.886 71	-12.4666
ip7	1220.744 496	-1.12	223.425 62	-20.4506
ip8	192.492 709	-0.865	351.389 58	-33.4185

occasions [0, 5] or [1, 6]. Any other range is indicative of a noncontinuous signal or artifact.

During the S6 run several simulated pulsar signals were injected into the data by applying a small force to the interferometer mirrors. Several outliers were due to such hardware injections (Table IV). The full list of injections including those too weak to be found by an all-sky search can be found in [25]. The hardware injection ip3 was exceptionally strong with a clear signature even in non-Gaussian band.

The recovery of the injections gives us confidence that no potential signals were missed. Manual followup has shown noninjection outliers to be caused by pronounced detector artifacts.

## V. CONCLUSIONS

We have performed the most sensitive all-sky search to date for continuous gravitational waves in the range

100–1500 Hz. We explored both positive and negative spindowns and placed upper limits on expected and unexpected sources. At the highest frequencies we are sensitive to neutron stars with an equatorial ellipticity as small as  $8 \times 10^{-7}$  and as far away as 1 kpc for favorable spin orientations. The use of a universal statistic allowed us to place upper limits on both Gaussian and non-Gaussian frequency bands. The maximum ellipticity a neutron star can theoretically support is at least  $1 \times 10^{-5}$  according to [26,27]. Our results exclude such maximally deformed pulsars above 200 Hz pulsar rotation frequency (400 Hz gravitational frequency) within 1 kpc.

A detection pipeline based on a *Loosely Coherent* algorithm was applied to outliers from our search. This pipeline was demonstrated to be able to detect simulated signals at the upper limit level for both Gaussian and non-Gaussian bands. Several outliers passed all stages of the coincidence pipeline; their parameters are shown in

Table III. However, manual examination revealed no true pulsar signals.

## ACKNOWLEDGMENTS

The authors gratefully acknowledge the support of the U. S. National Science Foundation (NSF) for the construction and operation of the LIGO Laboratory and Advanced LIGO as well as the Science and Technology Facilities Council (STFC) of the United Kingdom, the Max-Planck-Society (MPS), and the State of Niedersachsen/Germany for support of the construction of Advanced LIGO and construction and operation of the GEO600 detector. Additional support for Advanced LIGO was provided by the Australian Research Council. The authors gratefully acknowledge the Italian Istituto Nazionale di Fisica Nucleare (INFN), the French Centre National de la Recherche Scientifique (CNRS) and the Foundation for Fundamental Research on Matter supported by the Netherlands Organisation for Scientific Research, for the construction and operation of the Virgo detector and the creation and support of the EGO consortium. The authors also gratefully acknowledge research support from these agencies as well as by the Council of Scientific and Industrial Research of India, Department of Science and

Technology, India, Science & Engineering Research Board (SERB), India, Ministry of Human Resource Development, India, the Spanish Ministerio de Economía y Competitividad, the Conselleria d'Economia i Competitivitat and Conselleria d'Educació, Cultura i Universitats of the Govern de les Illes Balears, the National Science Centre of Poland, the European Commission, the Royal Society, the Scottish Funding Council, the Scottish Universities Physics Alliance, the Hungarian Scientific Research Fund (OTKA), the Lyon Institute of Origins (LIO), the National Research Foundation of Korea, Industry Canada and the Province of Ontario through the Ministry of Economic Development and Innovation, the Natural Science and Engineering Research Council Canada, Canadian Institute for Advanced Research, the Brazilian Ministry of Science, Technology, and Innovation, Fundação de Amparo à Pesquisa do Estado de São Paulo (FAPESP), Russian Foundation for Basic Research, the Leverhulme Trust, the Research Corporation, Ministry of Science and Technology (MOST), Taiwan and the Kavli Foundation. The authors gratefully acknowledge the support of the NSF, STFC, MPS, INFN, CNRS and the State of Niedersachsen/Germany for provision of computational resources.

- 
- [1] B. Abbott *et al.* (LIGO Scientific Collaboration), All-sky search for periodic gravitational waves in LIGO S4 data, *Phys. Rev. D* **77**, 022001 (2008).
  - [2] B. P. Abbott *et al.* (LIGO Scientific Collaboration), All-Sky LIGO Search for Periodic Gravitational Waves in the Early S5 Data, *Phys. Rev. Lett.* **102**, 111102 (2009).
  - [3] B. Abbott *et al.* (The LIGO and Virgo Scientific Collaboration), All-sky search for periodic gravitational waves in the full S5 data, *Phys. Rev. D* **85**, 022001 (2012).
  - [4] J. Aasi *et al.* (LIGO Scientific Collaboration and Virgo Collaboration), A search of the Orion spur for continuous gravitational waves using a “loosely coherent” algorithm on data from LIGO interferometers, *Phys. Rev. D* **93**, 042006 (2016).
  - [5] B. Abbott, M. Kramer, A. G. Lyne, *et al.* (LIGO Scientific Collaboration), Limits on Gravitational-Wave Emission from Selected Pulsars Using LIGO Data, *Phys. Rev. Lett.* **94**, 181103 (2005).
  - [6] B. Abbott, M. Kramer, A. G. Lyne, *et al.* (LIGO Scientific Collaboration), Upper limits on gravitational wave emission from 78 radio pulsars, *Phys. Rev. D* **76**, 042001 (2007).
  - [7] B. Abbott *et al.* (LIGO Scientific Collaboration), Searches for periodic gravitational waves from unknown isolated sources and Scorpius X-1: Results from the second LIGO science run, *Phys. Rev. D* **76**, 082001 (2007).
  - [8] B. Abbott *et al.* (LIGO Scientific Collaboration), Beating the spin-down limit on gravitational wave emission from the Crab pulsar, *Astrophys. J. Lett.* **683**, L45 (2008).
  - [9] B. P. Abbott *et al.* (LIGO Scientific Collaboration and Virgo Collaboration), Searches for gravitational waves from known pulsars with S5 LIGO data, *Astrophys. J.* **713**, 671 (2010).
  - [10] J. Abadie *et al.* (LIGO Scientific Collaboration), First search for gravitational waves from the youngest known neutron star, *Astrophys. J.* **722**, 1504 (2010).
  - [11] The Einstein@Home project is built upon the BOINC (Berkeley Open Infrastructure for Network Computing) architecture described at <http://boinc.berkeley.edu/>.
  - [12] B. Abbott *et al.* (LIGO Scientific Collaboration), Einstein@Home search for periodic gravitational waves in LIGO S4 data, *Phys. Rev. D* **79**, 022001 (2009).
  - [13] B. P. Abbott *et al.* (LIGO Scientific Collaboration), Einstein@Home search for periodic gravitational waves in early S5 LIGO data, *Phys. Rev. D* **80**, 042003 (2009).
  - [14] B. P. Abbott *et al.* (LIGO Scientific Collaboration), Einstein@Home all-sky search for periodic gravitational waves in LIGO S5 data, *Phys. Rev. D* **87**, 042001 (2013).
  - [15] V. Dergachev, On blind searches for noise dominated signals: A loosely coherent approach, *Classical Quantum Gravity* **27**, 205017 (2010).

- [16] V. Dergachev, A novel universal statistic for computing upper limits in ill-behaved background, *Phys. Rev. D* **87**, 062001 (2013).
- [17] B. Abbott *et al.* (LIGO Scientific Collaboration), LIGO: The Laser Interferometer Gravitational-Wave Observatory, *Rep. Prog. Phys.* **72**, 076901 (2009).
- [18] J. Abadie *et al.* (LIGO Scientific Collaboration and Virgo Collaboration), Sensitivity Achieved by the LIGO and Virgo Gravitational Wave Detectors during LIGO's Sixth and Virgo's Second and Third Science Runs, [arXiv:1203.2674](https://arxiv.org/abs/1203.2674).
- [19] J. Aasi *et al.* (LIGO Scientific Collaboration and Virgo Collaboration), Characterization of the LIGO detectors during their sixth science run, [arXiv:1410.7764](https://arxiv.org/abs/1410.7764).
- [20] V. Dergachev, LIGO Report No. LIGO-T050186, 2005, available in <https://dcc.ligo.org/>.
- [21] V. Dergachev, LIGO Report No. LIGO-T1000272, 2010, available in <https://dcc.ligo.org/>.
- [22] V. Dergachev and K. Riles, LIGO Report No. LIGO-T050187, 2005, available in <https://dcc.ligo.org/>.
- [23] V. Dergachev, Loosely coherent searches for sets of well-modeled signals, *Phys. Rev. D* **85**, 062003 (2012).
- [24] See Supplemental Material for <http://link.aps.org/supplemental/10.1103/PhysRevD.94.042002> for numerical values of upper limits.
- [25] J. Aasi *et al.* (LIGO Scientific Collaboration and Virgo Collaboration), Searches for continuous gravitational waves from nine young supernova remnants, *Astrophys. J.* **813**, 39 (2015).
- [26] C. J. Horowitz and K. Kadau, Breaking Strain of Neutron Star Crust and Gravitational Waves, *Phys. Rev. Lett.* **102**, 191102 (2009).
- [27] N. K. Johnson-McDaniel and B. J. Owen, Maximum elastic deformations of relativistic stars, *Phys. Rev. D* **88**, 044004 (2013).